5

Theoretical and Experimental Analysis of Flows and Heat Transfer Within Flat Mini Heat Pipe Including Grooved Capillary Structures

Zaghdoudi Mohamed Chaker, Maalej Samah and Mansouri Jed
University of Carthage – Institute of Applied Sciences and technology
Research Unit Materials, Measurements, and Applications
Tunisia

1. Introduction

Thermal management of electronic components must solve problems connected with the limitations on the maximum chip temperature and the requirements of the level of temperature uniformity. To cool electronic components, one can use air and liquid coolers as well as coolers constructed on the principle of the phase change heat transfer in closed space, i.e. immersion, thermosyphon and heat pipe coolers. Each of these methods has its merits and draw-backs, because in the choice of appropriate cooling one must take into consideration not only the thermal parameters of the cooler, but also design and stability of the system, durability, technology, price, application, etc.

Heat pipes represent promising solutions for electronic equipment cooling (Groll et al., 1998). Heat pipes are sealed systems whose transfer capacity depends mainly on the fluid and the capillary structure. Several capillary structures are developed in order to meet specific thermal needs. They are constituted either by an integrated structure of microchannels or microgrooves machined in the internal wall of the heat spreader, or by porous structures made of wire screens or sintered powders. According to specific conditions, composed capillary structures can be integrated into heat pipes.

Flat Miniature Heat Pipes (FMHPs) are small efficient devices to meet the requirement of cooling electronic components. They are developed in different ways and layouts, according to its materials, capillary structure design and manufacturing technology. The present study deals with the development of a FMHP concept to be used for cooling high power dissipation electronic components. Experiments are carried out in order to determine the thermal performance of such devices as a function of various parameters. A mathematical model of a FMHP with axial rectangular microchannels is developed in which the fluid flow is considered along with the heat and mass transfer processes during evaporation and condensation. The numerical simulations results are presented regarding the thickness distribution of the liquid film in a microchannel, the liquid and vapor pressures and velocities as well as the wall temperatures along the FMHP. By comparing the experimental results with numerical simulation results, the reliability of the numerical model can be verified.

2. Nomenclature

A	Constant in Eq. (8), Section,m²
C_p	Specific heat, J/kg.K
d	Side of the square microchannel, m
D_g	Groove height, m
D_h	Hydraulic diameter, m
f	Friction factor
g	Gravity acceleration, m/s²
h	Heat transfer coefficient, W/m².K
I	Current, A
Ja*	Modified Jacob number
k	Poiseuille number
l	Width, m
L	FMHP overall length, m
La	Laplace constant, m
l_c	Condenser width, m
L_c	Condenser length, m
l_e	Evaporator width, m
L_e	Evaporator length, m
$\dot{m}$	Mass flow rate, kg/s
m_1	Constant in Eq. (8)
m_2	Constant in Eq. (8)
m_3	Constant in Eq. (8)
N_g	Number of grooves
Nu	Nüsselt number
P	Pressure, N/m²
Pr	Prandtl number
q	Heat flux, W/m²
Q	Heat transfer rate, W
Q_a	Axial heat flux rate, W
r_c	Radius of curvature, m
Re	Reynolds number
R_{th}	Thermal resistance, K/W
S_g	Groove spacing, m
S	Heat transfer area, m²
S_g	Groove spacing, m
t	Thickness, m
T	Temperature, °C
T_c	Wall condenser temperature, °C
T_{ev}	Wall evaporator temperature, °C
T_f	Film temperature, °C
T_{sf}	Heat sink temperature, °C
T_w	Wall temperature, °C
V	Voltage, V
V_e	Velocity, m/s
w	Axial velocity, m/s
W	FMHP width, m
W_g	Groove width, m
z	Coordinate, m

Greek Symbols

α	Contact angle, °
β	Tilt angle, °
ΔT	Temperature difference = $T_{ev} - T_c$, K
Δh_v	Latent heat of vaporization, J/kg
ΔP	Pressure drop, N/m²
λ	Thermal conductivity, W/m.K
μ	Dynamic viscosity, kg/m.s
θ	Angle, °
ρ	Density, kg/m³
σ	Surface tension, N/m
τ	Shear stress, N/m²

Subscripts and superscripts

a	Adiabatic
b	Blocked
c	Condenser, Curvature
d	Dry
Cu	Copper
ev	Evaporator
eff	Effective
exp	Experimental
f	Film
il	Interfacial (liquid side)
iv	Interfacial (vapor side)
l	Liquid
lw	Liquid-Wall
max	Maximum
sat	Saturation
sf	Heat sink
t	Total
v	Vapor
vw	Vapor-Wall
w	Wall

3. Literature survey on mini heat pipes prototyping and testing

This survey concerns mainly the FMHPs made in metallic materials such as copper, aluminum, brass, etc. For the metallic FMHPs, the fabrication of microgrooves on the heat pipe housing for the wick structure has been widely adopted as means of minimizing the size of the cooling device. Hence, FMHPs include axial microgrooves with triangular, rectangular, and trapezoidal shapes. Investigations into FMHPs with newer groove designs have also been carried out, and recent researches include triangular grooves coupled with arteries, star and rhombus grooves, microgrooves mixed with screen mesh or sintered metal. The fabrication of narrow grooves with sharp corner angle is a challenging task for conventional micromachining techniques such as precision mechanical machining. Accordingly, a number of different techniques including high speed dicing and rolling method (Hopkins et al., 1999), Electric-Discharge-Machining (EDM) (Cao et al., 1997; Cao and Gao, 2002; Lin et al., 2002), CNC milling process (Cao and Gao, 2002; Gao and Cao, 2003; Lin et al., 2004; Zaghdoudi and Sarno, 2001, Zaghdoudi et al., 2004; Lefèvre et al., 2008), drawing and extrusion processes (Moon et al., 2003, 2004; Romestant et al., 2004; Xiaowu, 2009), metal forming process (Schneider et al., 1999a, 1999b, 2000; Chien et al., 2003), and flattening (Tao et al., 2008) have been applied to the fabrication of microgrooves. More recently, laser-assisted wet etching technique was used in order to machine fan-shaped microgrooves (Lim et al., 2008). A literature survey of the micromachining techniques and capillary structures that have been used in metallic materials are reported in table 1.

It can be seen from this overview that three types of grooved metallic FMHP are developed:

i. Type I: FMHPs with only axial rectangular, triangular or trapezoidal grooves (Murakami et al., 1987; Plesh et al., 1991; Sun and Wang, 1994; Ogushi and Yamanaka., 1994; Cao et al., 1997; Hopkins et al., 1999; Schneider et al., 1999a, 1999b, 2000; Avenas et al., 2001, Cao and Gao, 2002, Lin et al., 2002; Chien et al., 2003; Moon et al., 2003, 2004; Soo Yong and Joon Hong, 2003; Lin et al., 2004; Romestant et al., 2004; Zhang et al., 2004; Popova et al., 2006; Lefevre et al., 2008; Lim et al., 2008; Tao et al., 2008, Zhang et al., 2009; Xiaowu et al., 2009). These FMHPs allow for high heat fluxes for horizontal or thermosyphon positions (up to 150 W/cm²). However, in the majority of the cases, the thermal performances of such FMHP don't meet the electronic cooling requirements when the anti-gravity position is requested since the FMHP thermal performances are greatly altered for these conditions because the standard capillary grooves are not able to allow for the necessary capillary pumping able to overcome the pressure losses.
ii. Type II: FMHPs with mixed capillary structures such as grooves and sintered metal powder or grooves and screen meshes (Schneider et al.,1999a, 1999b, 2000; Zaghdoudi et al., 2004; Popova et al., 2005, 2006). Depending on the characteristics of the capillary structures such as the pore diameter, the wire diameter, the wire spacing and the number for screen wick layers, these FMHPs could meet the electronic cooling requirements especially for those applications where the electronic devices are submitted to forces such as gravity, acceleration and vibration forces (Zaghdoudi and Sarno, 2001). However, for standard applications, these FMHPs allow for low thermal performances (lower heat fluxes and higher thermal resistance) when compared to those delivered by the FMHPs of Type I.
iii. Type III: wickless FMHPs (Cao and Gao, 2002; Gao and Cao, 2003). These FMHPs utilize the concept of the boiling heat transfer mechanism in narrow space. These FMHPs can remove high heat flux rates with great temperature gradient between the hot source and the cold one.

Author	Micromachining Technique	Material	Capillary structure
Murakami et al. (1987)	—[a]	Brass	Triangular and rectangular grooves
Plesh et al. (1991)	—[a]	Copper	Axial and transverse rectangular grooves
Sun and Wang (1994)	—[a]	Aluminum	V-shaped axial grooves
Ogushi and Yamanaka (1994)	—[a]	Brass	Triangular and trapezoidal axial grooves
Cao et al. (1997)	Electric-discharge-machining (EDM)	Copper	Rectangular axial grooves
Hopkins et al. (1999)	Rolling method High-speed dicing saw	Copper	Trapezoidal diagonal grooves Rectangular axial grooves
Schneider et al. (1999a, 1999b, 2000)	Metal forming process	AlSiC	Triangular axial grooves
Avenas et al. (2001)	—[a]	Brass	Rectangular axial grooves
Zaghdoudi and Sarno (2001)	Milling process and sintering	Copper	Rectangular axial grooves and sintered powder wick
Cao and Gao (2002)	Milling process Electric Discharge Machining (EDM)	Aluminum Copper	Perpendicular network of crossed grooves Triangular axial grooves
Lin et al. (2002)	Electric-discharge-machining (EDM)	Copper	Rectangular axial grooves
Chien et al. (2003)	Metal forming process	Aluminum	Radial rectangular grooves
Gao and Cao (2003)	Milling process	Aluminum	Waffle-like cubes (protrusions)
Moon et al. (2003)	Drawing and extrusion process	Copper	Triangular and rectangular axial grooves with curved walls
Soo Yong and Joon Hong (2003)	—[a]	—[a]	Rectangular axial grooves with half circle shape at the bottom
Lin et al. (2004)	Etching, CNC milling, and sintering	Copper	Radial diverging grooves and sintered powder wick
Moon et al. (2004)	Drawing process	Copper	Triangular and rectangular grooves with incurved walls

Romestant et al. (2004)	Extrusion	Aluminum	Triangular axial grooves
Zaghdoudi et al. (2004)	Milling process	Copper	Triangular axial grooves and meshes
Zhang et al. (2004)	__[a]	Copper Stainless steel Copper	Rectangular axial grooves Trapezoidal axial grooves
Iavona et al. (2005)	Direct Bounded Copper technology	Copper/Alumina	Fiber mixed material of Al_2O_3 and SiO_2
Popova et al. (2005)	__[a]	Copper	Rectangular grooves machined in sintered copper structure
Popova et al. (2006)	__[a]	Copper	Rectangular grooves machined in sintered copper structure
Lefèvre et al. (2008)	Milling process	Copper	Rectangular axial grooves
Lim et al (2008)	Laser micromachining	Copper	Triangular axial grooves with curved walls
Tao et al. (2008)	Flattening of cylindrical finned tubes	Copper	Rectangular axial grooves with half circle shape at the bottom
Zhang et al. (2009)	__[a]	Copper	Radial diverging grooves
Xiaowu et al. (2009)	Extrusion-ploughing process	__[a]	V-shaped grooves

[a] Not specified in the reference

Table 1. Overview of the micromachining techniques of microgrooves for metallic FMHPs

From the studies published in open literature, the following points can be outlined:

i. The importance of the choice of the microchannel geometry. Indeed, according to the shape of a corner, the capillary pressure generated by the variation of the liquid-vapor interface curvature between the evaporator and the condenser, can be improved. An optimal shape of a corner permits to supply efficiently the evaporation zone in liquid, so that more heat power can be dissipated, and dry-out, which causes heat transfer degradation, can be avoided.
ii. The choice and the quantity of the introduced fluid in the microchannel play a primordial role for the good operation of the FMHP.
iii. Although the heat flux rates transferred by FMHPs with integrated capillary structure are low, these devices permit to transfer very important heat fluxes avoiding the formation of hot spots. Their major advantage resides in their small dimensions that permit to integrate them near the heat sources.

4. Literature survey on micro/mini heat pipe modeling

For FMHPs constituted of an integrated capillary structure including microchannels of different shapes, the theoretical approach consists of studying the flow and the heat transfer

in isolated microchannels. The effect of the main parameters, of which depends the FMHP operation, can be determined by a theoretical study. Hence, the influence of the liquid and vapor flow interaction, the fill charge, the contact angle, the geometry, and the hydraulic diameter of the microchannel can be predicted by models that analyze hydrodynamic aspect coupled to the thermal phenomena.

Khrustalev and Faghri (1995) developed a detailed mathematical model of low-temperature axially grooved heat pipes in which the fluid circulation is considered along with the heat and mass transfer processes during evaporation and condensation. The results obtained are compared to existing experimental data. Both capillary and boiling limitations are found to be important for the flat miniature copper-water heat pipes, which is capable of withstanding heat fluxes on the order of 40 W/cm² applied to the evaporator wall in the vertical position. The influence of the geometry of the grooved surface on the maximum heat transfer capacity of the miniature heat pipe is demonstrated.

Faghri and Khrustalev (1997) studied an enhanced flat miniature heat pipes with capillary grooves for electronics cooling systems, They survey advances in modeling of important steady-state performance characteristics of enhanced and conventional flat miniature axially-grooved heat pipes such as the maximum heat flow rate, thermal resistance of the evaporator, incipience of the nucleate boiling, and the maximum heat flux on the evaporator wall.

Khrustalev and Faghri (1999) analyze Friction factor coefficients for liquid flow in a rectangular microgroove coupled with the vapor flow in a vapor channel of a miniature two-phase device. The results show that the effect of the vapor-liquid frictional interaction on the liquid flow decreases with curvature of the liquid-vapor interface. Shear stresses at the liquid-vapor interface are significantly non-uniform, decreasing towards the center of the liquid-vapor meniscus.

Lefevre et al. (2003) developed a capillary two-phase flow model of flat mini heat pipes with micro grooves of different cross-sections. The model permits to calculate the maximum heat transfer capabilities and the optimal liquid charge of the FMHP. The results are obtained for trapezoidal and rectangular micro grooves cross-sections.

Launay et al. (2004) developed a detailed mathematical model for predicting the heat transport capability and the temperature distribution along the axial direction of a flat miniature heat pipe, filled with water. This steady-state model combines hydrodynamic flow equations with heat transfer equations in both the condensing and evaporating thin films. The velocity, pressure, and temperature distributions in the vapor and liquid phases are calculated. Various boundary conditions fixed to the FMHP evaporator and condenser have been simulated to study the thermal performance of the micro-heat-pipe array below and above the capillary limit. The effect of the dry-out or flooding phenomena on the FMHP performance, according to boundary conditions and fluid fill charge, can also be predicted.

Tzanova et al. (2004) presented a detailed analysis on maximum heat transfer capabilities of silicon-water FMHPs. The predictive hydraulic and thermal models were developed to define the heat spreader thermal performances and capillary limitations. Theoretical results of the maximal heat flux that could be transferred agree reasonably well with the experimental data and the developed model provides a better understanding of the heat transfer capability of FMHPs.

Angelov et al. (2005) proposed theoretical and modeling issues of FMHPs with parallelepipedal shape with regard to the capillary limit and the evaporator boiling limit. An improved model is suggested and it is compared with the simulation and experimental

results. The improved model implements a different analytically derived form of the friction factor-Reynolds number product (Poiseuille number). The simulated results with the proposed model demonstrate better coherence to the experiment showing the importance of accurate physical modeling to heat conduction behavior of the FMHP.

Shi et al. (2006) carried out a performance evaluation of miniature heat pipes in LTCC by numerical analysis, and the optimum miniature heat pipe design was defined. The effect of the groove depth, width and vapor space on the heat transfer capacity of miniature heat pipes was analyzed.

Do et al. (2008) developed a mathematical model for predicting the thermal performance of a FMHP with a rectangular grooved wick structure. The effects of the liquid-vapor interfacial shear stress, the contact angle, and the amount of liquid charge are accounted for in the present model. In particular, the axial variations of the wall temperature and the evaporation and condensation rates are considered by solving the one-dimensional conduction equation for the wall and the augmented Young-Laplace equation, respectively. The results obtained from the proposed model are in close agreement with several existing experimental data in terms of the wall temperatures and the maximum heat transport rate. From the validated model, it is found that the assumptions employed in previous studies may lead to significant errors for predicting the thermal performance of the heat pipe. Finally, the maximum heat transport rate of a FMHP with a grooved wick structure is optimized with respect to the width and the height of the groove by using the proposed model. The maximum heat transport rate for the optimum conditions is enhanced by approximately 20%, compared to existing experimental results.

Do and Jang (2010) investigated the effect of water-based Al2O3 nanofluids as working fluid on the thermal performance of a FMHP with a rectangular grooved wick. For the purpose, the axial variations of the wall temperature, the evaporation and condensation rates are considered by solving the one-dimensional conduction equation for the wall and the augmented Young-Laplace equation for the phase change process. In particular, the thermophysical properties of nanofluids as well as the surface characteristics formed by nanoparticles such as a thin porous coating are considered. From the comparison of the thermal performance using both water and nanofluids, it is found that the thin porous coating layer formed by nanoparticles suspended in nanofluids is a key effect of the heat transfer enhancement for the heat pipe using nanofluids. Also, the effects of the volume fraction and the size of nanoparticles on the thermal performance are studied. The results show the feasibility of enhancing the thermal performance up to 100% although water-based Al2O3 nanofluids with the concentration less than 10% is used as working fluid. Finally, it is shown that the thermal resistance of the nanofluid heat pipe tends to decrease with increasing the nanoparticle size, which corresponds to the previous experimental results.

5. Experimental study

5.1 FMHP fabrication and filling procedure

A FMHP has been designed, manufactured, and tested. The design parameters are based on some electronic components that require high power dissipation rate. The design is subjected to some restrictions such as the requirements for size, weight, thermal resistance, working temperature, and flow resistance. For comparison purposes, a solid heat sink that has the same size but more weight than the FMHP is also tested. The test sample is made of the same copper and their dimensions are 100 mm length, 50 mm width, and 3 mm

thickness. The FMHP body is manufactured in two halves. Manufacturing of the FMHP begins with the capillary grooves being mechanically machined by a high speed dicing process in the first half (2 mm thick) and the second half, which consists of a copper cover slip 1 mm thick, is bonded to the first half by an electron beam welding process. The heat pipe charging tube (2 mm diameter), from which the fluid working is introduced, is bounded to the heat pipe end by a classic welding technique. The geometrical dimensions of the FMHP are indicated in table 2 and in Fig. 1. A view of the microchannels is shown in Fig. 2.

Filling the FMHP presents one of the greatest challenges. In this study, a boiling method is used for the filling purpose. The filling assembly includes a vacuum system, a boiler filled with distilled water, vacuum tight electrovalves, a burette for a precise filling of the FMHP and a tubular adapter. The degassing and charging procedure consists of the following steps: (i) degassing water by boiling process, (ii) realizing a vacuum in the complete set-up, (iii) charging of the burette, and (iv) charging of the FMHP. An automatic process controls the whole steps. After charging the FMHP, the open end (a 2 mm diameter charging tube) is sealed. The amount of liquid is controlled by accurate balance. Indeed, the FMHP is weighed before and after the fill charging process and it is found that the optimum fill charge for the FMHP developed in this study is 1.2 ml.

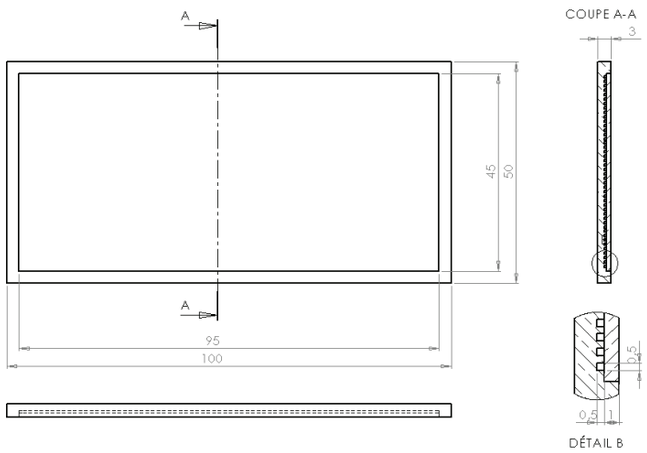

Fig. 1. Sketch of the FMHPs

Fig. 2. View of the microchannels

FMHP width, W	50
FMHP overall length, L_t	100
FMHP thickness, t	3
Microchannel height, D_g	0.5
Microchannel width W_g (mm)	0.5
Microchannel spacing S_g (mm)	1
Overall width of the microchannels	45
Overall length of the microchannels (mm)	95
Number of the microchannels, N_g	47

Dimensions are in mm.

Table 2. Main geometrical parameters of the FMHP

5.2 Experimental set-up and procedures

Heat input is delivered by an electric resistance cartridge attached at one end of the FMHP and it is provided on the grooved side of the FMHP. The power input to the heater is controlled through a variable transformer so that a constant power is supplied to the heated section, and the voltage and current are measured using digital voltmeter and ammeter. Both the evaporator and the adiabatic sections are thermally insulated. The heat loss from the insulation surface to the ambient is determined by evaluating the temperature difference and the heat transfer coefficient of natural convection between the insulated outer surface and ambient. Heat is removed from the FMHP by a water cooling system. A thermally conductive paste is used to enhance the heat transfer between the copper FMHP and the aluminum blocks. The lengths of the evaporator, adiabatic, and condenser zones are L_e = 19 mm, L_a = 35 mm, and L_c = 45 mm, respectively. The temperature distribution across the surface of the FMHP and the copper plate is obtained using 6 type-J surface mounted thermocouples. The thermocouples are located, respectively at 5, 15, 27, 42, 60, and 90 mm from the end cap of the evaporator section. In order to measure the evaporator and condenser temperatures, grooves are practiced on the FMHP wall and thermocouples are inserted along the grooves. The thermocouples locations and the experimental set-up are shown in Figs. 3 and 4.

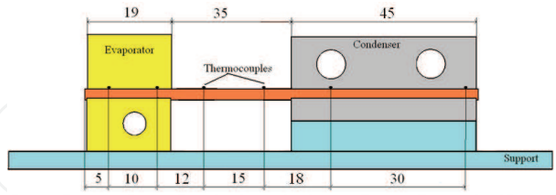

Fig. 3. Thermocouple locations

The experimental investigation focuses on the heat transfer characteristics of the FMHP at various heat flux rates, Q, and operating temperatures, T_{sf}. Input power is varied in increments from a low value to the power at which the evaporator temperature starts to increase rapidly. In the process, the temperature distribution of the heat pipe along the longitudinal axis is observed and recorded. All experimental data are obtained with a systematic and consistent methodology that is as follows. First, the flat miniature heat pipe is positioned in the proper orientation and a small heat load is applied to the evaporator section. Secondly, the heat sink operating temperature is obtained and maintained by adjusting the cooling water flow to the aluminum heat sink. Once the heat sink temperature is obtained, the

system is allowed to reach steady-state over 10-15 minutes. After steady-state is reached, temperature readings at all thermocouples are recorded and power to the evaporator is increased by a small increment. This cycle is repeated until the maximum capillary limit is reached which is characterized by a sudden and steady rise of the evaporator temperature.

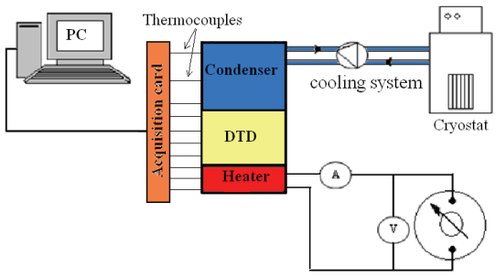

Fig. 4. Experimental set-up

The data logger TC-08 acquisition system is used to make all temperature measurements. The type J thermocouples are calibrated against a precision digital RTD and their accuracy over the range of interest is found to be within 0.5 °C. In the steady-state, the wall thermocouples fluctuate within 0.2 °C. The uncertainty of the thermocouples is 0.3°C + 0.03 × 10^{-2} T, where T is the measured temperature. The uncertainty of the thermocouples locations is within 0.5 mm in the heat pipe axial direction. A pair of multimeters is used to determine and record the power supplied to the resistors. The first multimeter is used to measure voltage across the film resistor and has an accuracy of 2 % of true voltage while the second measures the AC current and has accuracy 2 % of true AC current. The power input to the electric heater is calculated using the measured current and voltage (Q = V × I). The thermal resistance, R_{th}, of the heat pipe is defined as the ratio of the temperature drop, $\Delta T = T_{ev} - T_c$, across the heat pipe to the input heat power Q.

5.3 Experimental results and analysis

5.3.1 Combined effects of the heat input power and the heat sink temperature

Figs 5a to 5c illustrate typical steady temperature profiles for the FMHP prototypes for 10 W to 60 W at a heat sink temperature, T_{sf}, of 10 °C, 20 °C, and 40 °C, when it is oriented horizontally. The maximum evaporator temperature and temperature gradients for the FMHP are considerably smaller than those obtained for copper plate (Fig. 5d). For instance, for T_{sf} = 40 °C, at an input power of 60 W, the maximum steady-state evaporator temperature for the FMHP is nearly 100 °C, while for the copper plate the maximum evaporator temperature is 160°C. This results in a decrease in temperature gradients of approximately 60 °C. The heat source-heat sink temperature difference, $\Delta T = T_{ev} - T_c$, for T_{sf} = 40 °C when the FMHP is oriented horizontally, are plotted as a function of the applied heat flux rate in Fig. 6. Also shown for comparison is the heat source-heat sink temperature difference for a copper plate. The maximum evaporator temperature and temperature gradients for the FMHP are considerably smaller than those obtained for the copper plate. As shown in Fig. 6, the heat pipe operation reduces the slope of the temperature profile for the FMHP. This gives some indication of the ability of such FMHP to reduce the thermal gradients or localized hot spots. The size of the source-sink temperature difference for the FMHP increases in direct proportion of the input heat flux rate and varies from almost 10 °C at low power levels to approximately 50 °C at input power levels of approximately 60 W.

This plot again shows the effectiveness of the enhanced FMHP and clearly indicates the temperature reduction level that can be expected at higher heat flux rates prior to dry-out.
The effective end cap to end cap thermal resistance of the FMHP is given in Fig. 7. Effective end cap to end cap thermal resistance, R_{tht}, defined here as the overall en cap to end cap temperature drop divided by the total applied heat load, Q. A common characteristic of the thermal resistance presented here is that the thermal resistance of the FMHP is high at low heat loads as a relatively thick liquid film resides in the evaporator. However, this thermal resistance decreases rapidly to its minimum value as the applied heat load is increased. This minimum value corresponds to the capillary limit. When the applied heat flux rate becomes higher than the capillary limit, the FMHP thermal resistance increases since the evaporator becomes starved of liquid. This is due to the fact that the capillary pumping cannot overcome the pressure losses within the FMHP. The decrease of the FMHP thermal resistance is attributed mainly to the decrease of the evaporator thermal resistance when the heat flux increases. Indeed, increasing the heat flux leads to the enhancement evaporation process in the grooves. The decrease of R_{tht} is observed when the evaporation process is dominated by the capillary limit. However, for heat flux rates higher than the maximum capillary limit, intensified boiling process may occur in the capillary structure, and consequently the evaporator thermal resistance increases. This results in an increase of the overall FMHP thermal resistance.

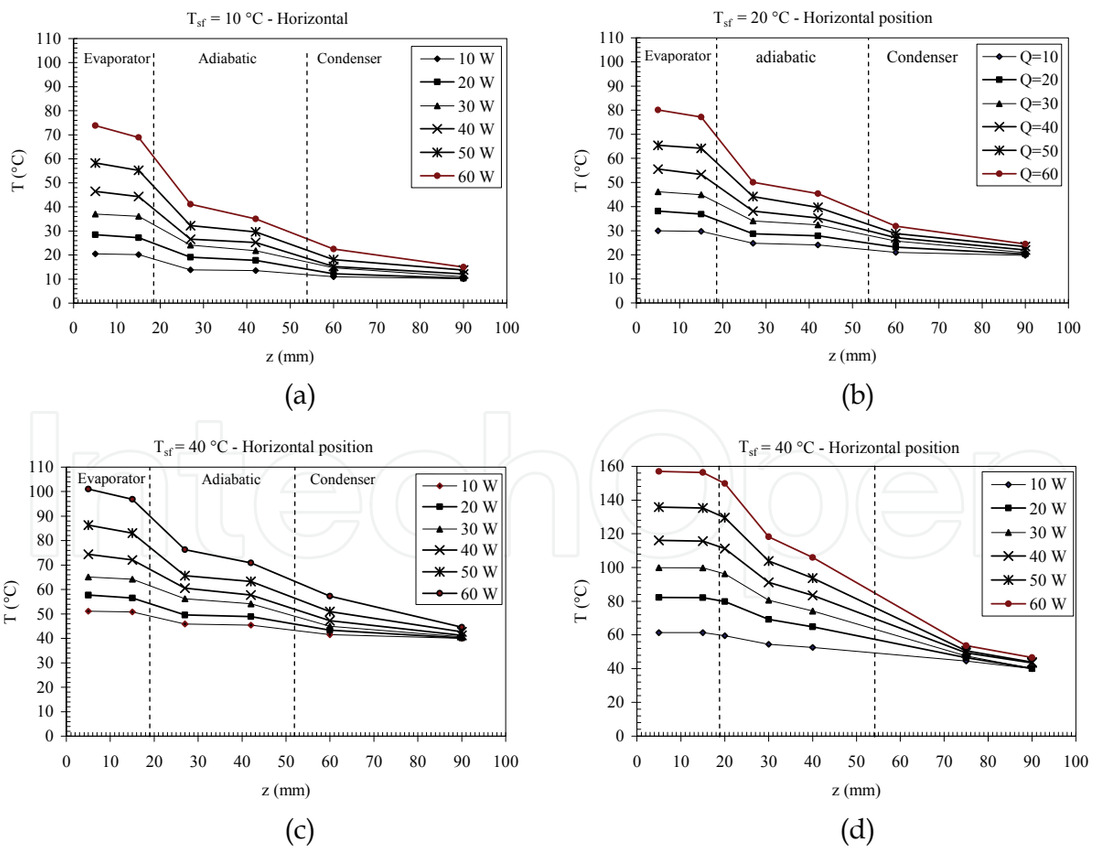

Fig. 5. FMHP axial temperature profile obtained for a) T_{sf} = 10 °C, b) T_{sf} =20 °C, and c) T_{sf} = 40 °C, and copper plate axial temperature profile for T_{sf} = 40 °C (d)

It is also noticed that for a given heat flux rate the thermal resistance decreases as the heat sink temperature increases and the capillary limit, Q_{max}, increases. The increase in Q_{max} with T_{sf} is due to the decrease of the overall pressure drop ($\Delta P_l + \Delta P_v$). Indeed, when T_{sf} increases, the vapor temperature, T_{sat}, increases too. This results in a dramatic decrease of the vapor friction factor and consequently the vapor pressure drop ΔP_v decreases. However, the liquid pressure drop, ΔP_l increases with T_{sf} because an augmentation of the liquid mass flow rate is allowed by a decrease of the liquid friction factor with T_{sf}. Since the increase in ΔP_l is lower than the decrease in ΔP_v, the overall pressure drop ($\Delta P_l + \Delta P_v$) decrease. As shown in Fig. 7, the effect the heat sink temperature on the FMHP thermal resistance is effective when the heat input power is greater than the capillary limit.

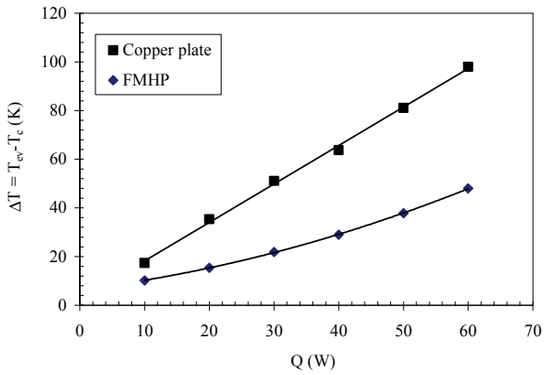

Fig. 6. $T_{ev} - T_c$ variations Vs. Q

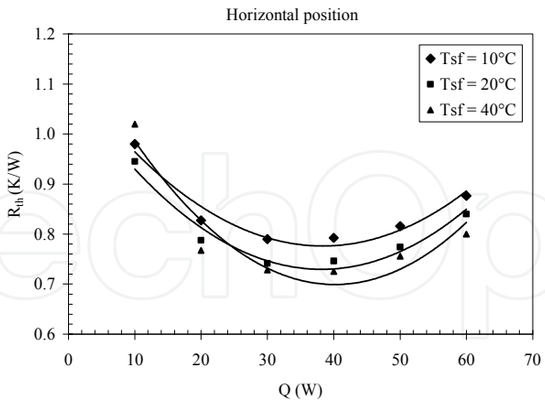

Fig. 7. FMHP thermal resistance Vs. Q, for

In order to quantify the experimental results better, additional data are taken from which an effective FMHP conductivity, λ_{eff}, could be calculated using Fourier's law. The axial heat flux rate, that is, the heat transported through the FMHP in the direction of the grooves, is computed by dividing the input power by the FMHP cross-sectional area. This value is then divided by the source-sink temperature difference. The obtained result is then multiplied by

the linear distance between the points at which the source and sink temperatures are measured. As depicted in Fig. 8, the increasing trend observed in the effective thermal conductivity of the FMHP results from the decreasing temperature gradient occurring at high heat flux rates which makes the heat pipes perform more effectively.

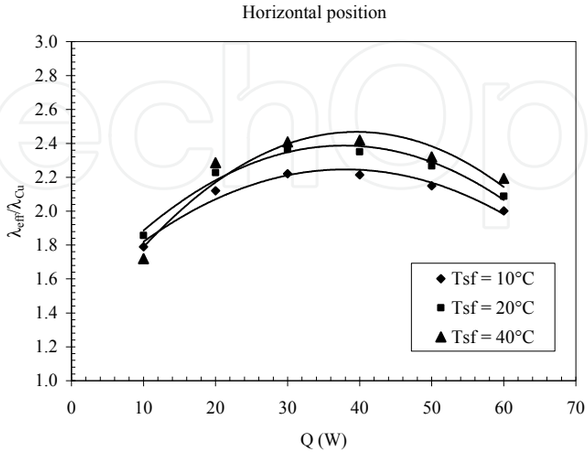

Fig. 8. Effective thermal conductivity enhancement variations Vs. Q, for different heat sink temperatures

The heat transfer coefficients in the evaporator and condenser zones are calculated according to the following expressions

$$h_{ev} = \frac{1}{\frac{(T_{ev} - T_{sat})}{q_{ev}} - \frac{t_w}{\lambda_w}} \quad (1)$$

$$h_c = \frac{1}{\frac{(T_{sat} - T_c)}{q_c} - \frac{t_w}{\lambda_w}} \quad (2)$$

q_{ev} and q_c are the heat fluxes calculated on the basis the evaporator and condenser heat transfer areas. t_w and λ_w are the thickness and the thermal conductivity of the wall, respectively.

The variations of the evaporation and condensation heat transfer as a function of the heat input power are depicted in Fig. 9, for different heat sink temperatures. The evaporation heat transfer coefficients are larger than the condensation ones. For a given heat sink temperature, the evaporation heat transfer coefficient exhibits a maximum which corresponds to the capillary limit, Q_{max}. The degradation of the evaporation process is caused by the fact that, for heat input powers which are higher than the capillary limit, the evaporator becomes starved of liquid and dry-out occurs since the capillary pumping is not sufficient for these conditions to overcome the liquid and vapor pressure losses. The condensation heat transfer coefficient increases with the heat input power, Q. This is due to the fact that the FMHP is correctly filled, and the blocking zone at the end of the condenser section is not large. For a given heat input power, the evaporation heat transfer coefficient

increases with the heat sink temperature, however, the condensation heat transfer coefficient seems to decrease when the heat sink temperature increases. Hence, the evaporation process in the grooves is enhanced when the heat sink temperature increases; meanwhile the condensation process is altered.

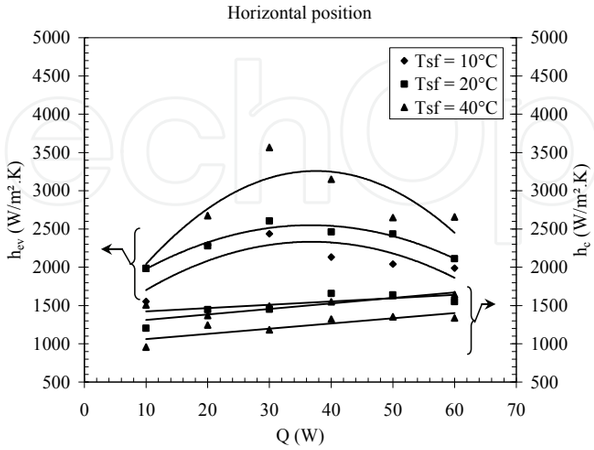

Fig. 9. Evaporation and condensation heat transfer coefficients Vs. Q, for different heat sink temperatures

5.3.2 Combined effects of the heat input power and the tilt angle

To determine the significance of the gravitational forces, experiments are carried out with different FMHP orientations: horizontal, thermosyphon, and anti-gravity positions. The heat sink temperature is fixed at T_{sf} = 40°C. The FMHP thermal resistances variations as a function of the heat input power are depicted in Fig. 10, for different FMHP orientations. For heat flux rates Q > 40 W, the FMHP thermal resistances are nearly the same for the different positions (if we consider the uncertainties on thermal resistance). However, for heat flux rates Q < 40 W, the FMHP becomes sensitive to the orientation. The Anti-gravity position exhibits the highest thermal resistances, while the thermosyphon and the horizontal positions exhibit similar thermal resistances which are lower than those obtained for the anti-gravity position.

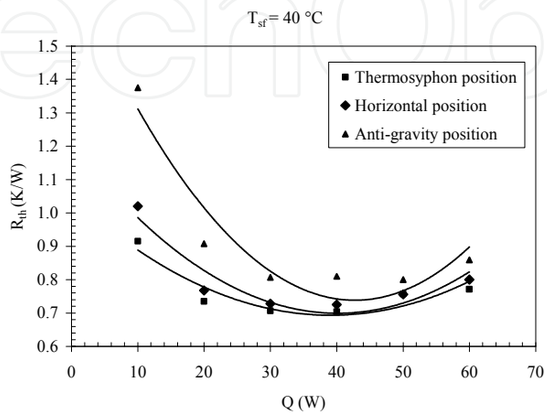

Fig. 10. FMHP thermal resistance Vs. Q, for different orientations

In Fig. 11 are depicted the variations of the ratio of the effective thermal conductivity, λ_{eff}, to the copper thermal conductivity, λ_{Cu}, as a function of the heat power input. The enhancement of the effective thermal conductivity of the FMHP amounts to an increase of nearly 240 percent for an input heat flux rate of about 40 W, for the horizontal and thermosyphon positions, however, for the anti-gravity position, the enhancement is lower and varies from nearly 30% for a heat input power of 10 W to 220% for a heat input power of 40 W, and decreases to 200% for Q = 60 W.

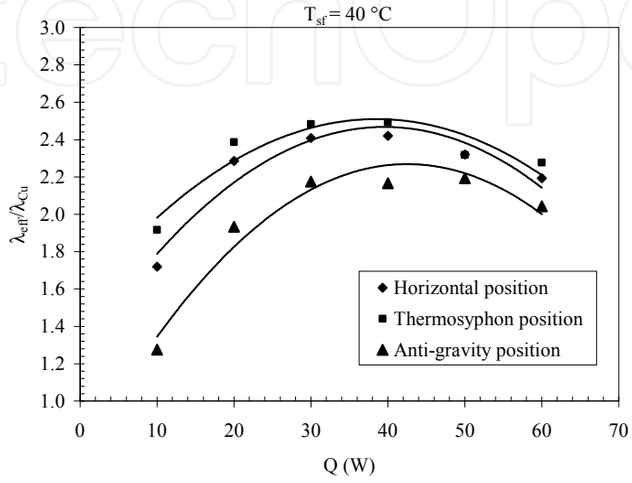

Fig. 11. Effective thermal conductivity enhancement variations as a function of Q, for different orientations (T_{sf} = 40 °C)

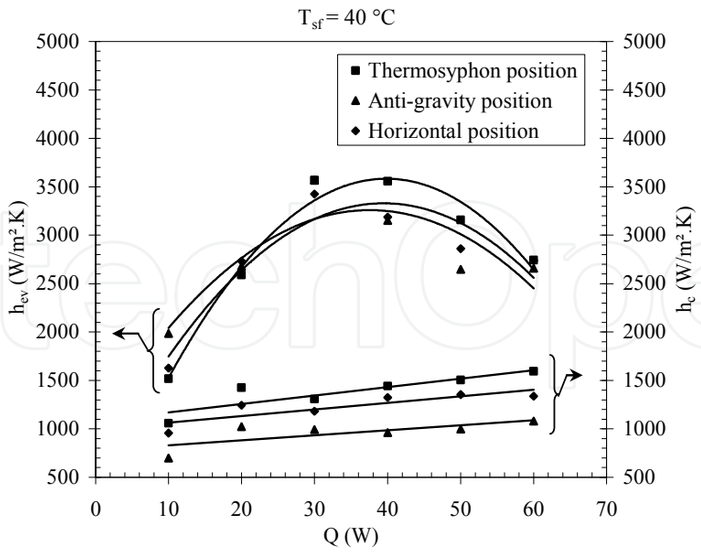

Fig. 12. Evaporation and condensation heat transfer coefficient Vs. Q, for different orientations (T_{sf} = 40 °C)

Fig. 12 shows the variations of the evaporator and condensation heat transfer coefficients as a function of the heat input power, Q. As it can be noticed, the evaporator heat transfer

coefficients are not very sensitive to the FMHP orientation (if we consider the uncertainties). We can also notice that for heat input powers, which are higher than the capillary limit, the evaporator heat transfer coefficients are higher than those obtained for the horizontal and anti-gravity positions. However, the condensation heat transfer coefficient is sensitive to the orientation. These results can be explained by the liquid distribution inside the FMHP which is dependent on its orientation since the thermosyphon position is favorable to the return of the liquid to the evaporator.

5.3.3 Heat transfer law

In order to quantify the heat transfer mechanisms in the evaporator and condenser zones, we have processed the experimental data in dimensionless numbers in order to obtain heat transfer laws. The dimensionless analysis is carried out on the basis of Vaschy-Backingham theorem (or π theorem). The heat transfer coefficients in the evaporator and condenser zones are calculated according to equations (1) and (2).The following dimensionless numbers are evidenced from the π analysis:

i. the Laplace constant (obtained for Bond number equal to unity), La

$$La = \sqrt{\frac{\sigma}{(\rho_l - \rho_v)g}} \tag{3}$$

where σ is the liquid surface tension. ρ_l and ρ_v are the liquid and vapor densities, respectively. g is the gravity acceleration.

ii. the Reynolds number, Re

$$Re = \frac{\rho_l V_e La}{\mu_l} = \frac{\dot{m}}{\mu_l S} = \frac{Q}{\mu_l S \Delta h_v} = \frac{q}{\mu_l \Delta h_v} \tag{4}$$

where V_e is the liquid or the vapor velocity. μ_l is the liquid dynamic viscosity, and Δh_v is the latent heat. S is the heat transfer area in the evaporator ($L_e \times l_e$) or condenser section ($L_c \times l_c$), Q is the heat flux rate, and q is the heat flux transferred in the evaporator or the condenser zone.

iii. the Prandtl number, Pr

$$Pr = \frac{\mu_l C_{pl}}{\lambda_l} \tag{5}$$

where C_{pl} is the liquid specific heat, and λ_l is the liquid thermal conductivity.

iv. the Nüsselt number, Nu

$$Nu = \frac{h\, La}{\lambda_l} \tag{6}$$

where h is the heat transfer coefficient in the evaporator or condenser section.

v. the modified Jakob number, Ja*

$$Ja^* = \frac{\rho_l}{\rho_v} \frac{C_{pl} T_{sat}}{\Delta h_v} \tag{7}$$

Hence, the heat transfer coefficients can be calculated by

$$Nu = A\,Re^{m_1}\,Pr^{m_2}\,Ja^{*m_3} \quad (8)$$

A, m_1, m_2, and m_3 are constant, which are determined from the experimental results. For the evaporation heat transfer, relation (8) is calculated by taking the liquid physical properties at the saturation temperature and the vapor physical properties at the film temperature ($T_f = (T_{sat}+T_w)/2$). For condensation heat transfer, the liquid and vapor physical properties are determined by considering the film and saturation temperatures, respectively.
The constants of equation (8) are determined from the experimental data by a linear regression analysis, for the evaporation and the condensation phenomena. It is found that the heat transfer law proposed by equation (8), the experimental results are well correlated when considering A = 902, m_1 = 0.825, m_2 = 0.333, m_3 = -0.999, and m_4 = -0.020, for the evaporation phenomena, and A = 2.165×10^{-12}, m_1 = 1.001, m_2 = -0.032, m_3 = 2.644, and m_4 = 1.907, for the condensation phenomena. The variations of the calculated Nüsselt number as a function of the Nüsselt number obtained experimentally are depicted in Fig. 13. As it can be seen from Fig. 13, the experimental Nüsselt number for the heat transfer by evaporation is well represented by equation (8). For the evaporation heat transfer, the coefficient of correlation is 0.751 and the deviation from the experimental results is ± 20%. For the condensation heat transfer law, the experimental results are very well represented by equation (8) with a coefficient of correlation of 0.978, and the deviation from the experimental results is ± 10%.

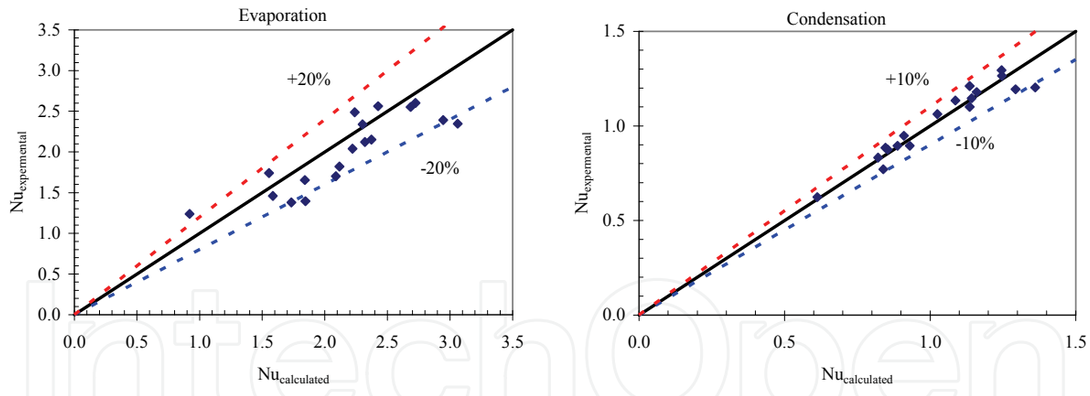

Fig. 13. Comparison between the Nusselt number obtained from the experimental results and that obtained from equation (8) for (a) the evaporation heat transfer, (b) the condensation heat transfer

6. FMHP modeling

6.1 Equations of the model

The section of the FMHP is illustrated by Fig. 1 (square microchannels with $D_g = W_g = d$). The liquid accumulates in the corners and forms four meniscuses (Fig. 14). Their curvature radius, r_c, is related to the difference of pressure, between vapor and liquid phase, by the Laplace-Young equation.

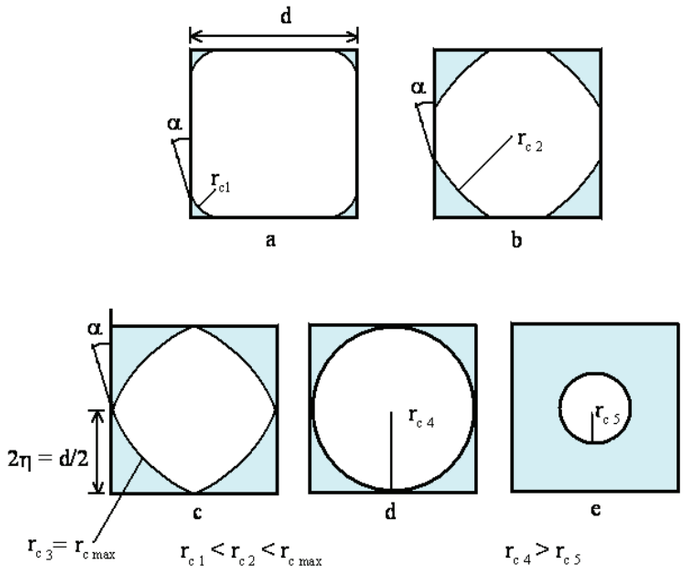

Fig. 14. Evolution of the curvature radius along a microchannel

In the evaporator and adiabatic zones, the curvature radius, in the parallel direction of the microchannel axis, is lower than the one perpendicular to this axis. Therefore, the meniscus is described by only one curvature radius. In a given section, r_c is supposed constant. The axial evolution of r_c is obtained by the differential of the Laplace-Young equation. The part of wall that is not in contact with the liquid is supposed dry and adiabatic.

In the condenser, the liquid flows toward the microchannel corners. There is a transverse pressure gradient, and a transverse curvature radius variation of the meniscus. The distribution of the liquid along a microchannel is presented in Fig. 14.

The microchannel is divided into several elementary volumes of length, dz, for which, we consider the Laplace-Young equation, and the conservation equations written for the liquid and vapor phases as it follows

Laplace-Young equation

$$\frac{dP_v}{dz} - \frac{dP_l}{dz} = -\frac{\sigma}{r_c^2}\frac{dr_c}{dz} \tag{9}$$

Liquid and vapor mass conservation

$$\frac{d\left(\rho_l\, w_l\, A_l\right)}{dz} = \frac{1}{\Delta h_v}\,\frac{dQ}{dz} \tag{10}$$

$$\frac{d\left(\rho_v\, w_v\, A_v\right)}{dz} = -\frac{1}{\Delta h_v}\,\frac{dQ}{dz} \tag{11}$$

Liquid and vapor momentum conservation

$$\rho_l \frac{d(A_l w_l^2)}{dz}dz = \frac{d(A_l P_l)}{dz}dz + A_{il}\left|\tau_{il}\right| + A_{lw}\left|\tau_{lw}\right| - \rho_l\, g\, A_l \sin\beta\, dz \tag{12}$$

$$\rho_v \frac{d(A_v w_v^2)}{dz} dz = -\frac{d(A_v P_v)}{dz} dz - |\tau_{il}| A_{il} - |\tau_{vw}| A_{vw} - \rho_v g A_v \sin\beta \, dz \quad (13)$$

Energy conservation

$$\lambda_w \frac{\partial^2 T_w}{\partial z^2} - \frac{h}{t_w}(T_w - T_{sat}) = -\frac{1}{1 \times t_w} \frac{dQ}{dz} \quad (14)$$

The quantity dQ/dz in equations (10), (11), and (14) represents the heat flux rate variations along the elementary volume in the evaporator and condenser zones, which affect the variations of the liquid and vapor mass flow rates as it is indicated by equations (10) and (11). So, if the axial heat flux rate distribution along the microchannel is given by

$$Q = \begin{cases} Q_a \, z/L_e & 0 \le z \le L_e \\ Q_a & L_e < z < L_e + L_a \\ Q_a \left(1 + \dfrac{L_e + L_a - z}{L_c - L_b}\right) & L_e + L_a \le z \le L_t - L_b \end{cases} \quad (15)$$

we get a linear flow mass rate variations along the microchannel.
In equation (15), h represents the heat transfer coefficient in the evaporator, adiabatic and condenser sections. For these zones, the heat transfer coefficients are determined from the experimental results (section 5.3.3). Since the heat transfer in the adiabatic section is equal to zero and the temperature distribution must be represented by a mathematical continuous function between the different zones, the adiabatic heat transfer coefficient value is chosen to be infinity.
The liquid and vapor passage sections, A_l, and A_v, the interfacial area, A_{il}, the contact areas of the phases with the wall, A_{lp} and A_{vp}, are expressed using the contact angle and the interface curvature radius by

$$A_l = 4 * r_c^2 \left(\sin^2\theta - \theta + \frac{\sin 2\theta}{2}\right) \quad (16)$$

$$A_v = d^2 - A_l \quad (17)$$

$$A_{il} = 8 \times \theta \times r_c \times dz \quad (18)$$

$$A_{lw} = \frac{16}{\sqrt{2}} r_c \sin\theta \, dz \quad (19)$$

$$A_{vw} = \left(4 \times d - \frac{16}{\sqrt{2}} r_c \sin\theta\right) dz \quad (20)$$

$$\theta = \frac{\pi}{4} - \alpha \quad (21)$$

The liquid-wall and the vapor-wall shear stresses are expressed as

$$\tau_{lw} = \frac{1}{2}\rho_l w_l^2 f_l \,,\; f_l = \frac{k_l}{R_{e_l}} \;,\; R_{el} = \frac{\rho_l w_l D_{hlw}}{\mu_l} \tag{22}$$

$$\tau_{vw} = \frac{1}{2}\rho_v w_v^2 f_v \,, f_v = \frac{k_v}{R_{ev}} \;,\; R_{ev} = \frac{\rho_v w_v D_{hvw}}{\mu_v} \tag{23}$$

Where k_l and k_v are the Poiseuille numbers, and D_{hlw} and D_{hvw} are the liquid-wall and the vapor-wall hydraulic diameters, respectively.
The hydraulic diameters and the shear stresses in equations (22) and (23) are expressed as follows

$$D_{hlw} = \frac{\sqrt{2}\times r_c\left(\sin^2\theta - \theta + \frac{\sin 2\theta}{2}\right)}{\sin\theta} \tag{24}$$

$$D_{hvw} = \frac{d^2 - 4r_c^2\left(\sin^2\theta - \theta + \frac{\sin 2\theta}{2}\right)}{d - \frac{4}{\sqrt{2}}\sin\theta\times r_c} \tag{25}$$

$$\tau_{lw} = \frac{1}{2}\frac{k_l w_l \mu_l \sin\theta}{2\sqrt{2}\left(\sin^2\theta - \theta + \frac{\sin\theta}{2}\right)r_c} \tag{26}$$

$$\tau_{vw} = \frac{k_v w_v \mu_v\left(d - \left(\frac{4}{\sqrt{2}}\sin\theta\right)r_c\right)}{2\left(d^2 - 4r_c^2\left(\sin^2\theta - \theta + \frac{\sin\theta}{2}\right)\right)} \tag{27}$$

The liquid-vapor shear stress is calculated by assuming that the liquid is immobile since its velocity is considered to be negligible when compared to the vapor velocity ($w_l << w_v$). Hence, we have

$$\tau_{il} = \frac{1}{2}\frac{\rho_v w_v^2 k_v}{R_{eiv}} \;,\; R_{eiv} = \frac{\rho_v |w_v| D_{hiv}}{\mu_v} \tag{28}$$

where D_{hiv} is the hydraulic diameter of the liquid-vapor interface. The expressions of D_{hiv} and τ_{iv} are

$$D_{hi} = \frac{d^2 - 4r_c^2\left(\sin^2\theta - \theta + \frac{\sin 2\theta}{2}\right)}{2\;\theta\; r_c} \tag{29}$$

$$\tau_{il} = \frac{k_v \theta\; r_c w_v \mu_v}{d^2 - 4r_c^2\left(\sin^2\theta - \theta + \frac{\sin 2\theta}{2}\right)} \tag{30}$$

The equations (9-14) constitute a system of six first order differential, nonlinear, and coupled equations. The six unknown parameters are: r_c, w_l, w_v, P_l, P_v, and T_w. The integration starts in the beginning of the evaporator (z = 0) and ends in the condenser extremity ($z = L_t - L_b$), where L_b is the length of the condenser flooding zone. The boundary conditions for the adiabatic zone are the calculated solutions for the evaporator end. In z = 0, we use the following boundary conditions:

$$\begin{cases} r_c\big|^0 = r_{cmin} & \text{(a)} \\ w_l\big|^0 = w_v\big|^0 = 0 & \text{(b)} \\ P_v\big|^0 = P_{sat}(T_v) & \text{(c)} \\ P_l\big|^0 = P_v - \dfrac{\sigma}{r_{cmin}} & \text{(d)} \end{cases} \tag{31}$$

The solution is performed along the microchannel if r_c is higher than r_{cmin}. The coordinate for which this condition is verified, is noted L_{as} and corresponds to the microchannel dry zone length. Beyond this zone, the liquid doesn't flow anymore. Solution is stopped when $r_c = r_{cmax}$, which is determined using the following reasoning: the liquid film meets the wall with a constant contact angle. Thus, the curvature radius increases as we progress toward the condenser (Figs. 14a and 14b). When the liquid film contact points meet, the wall is not anymore in direct contact with vapor. In this case, the liquid configuration should correspond to Fig. 14c, but actually, the continuity in the liquid-vapor interface shape imposes the profile represented on Figure 14d. In this case, the curvature radius is maximum. Then, in the condenser, the meniscus curvature radius decreases as the liquid thickness increases (Fig. 14e). The transferred maximum power, so called capillary limit, is determined if the junction of the four meniscuses starts precisely in the beginning of the condenser.

6.2 Numerical results and analysis

In this analysis, we study a FMHP with the dimensions which are indicated in Table 1. The capillary structure is composed of microchannels as it is represented by the sketch of Fig. 1. The working fluid is water and the heat sink temperature is equal to 40 °C. The conditions of simulation are such as the dissipated power is varied, and the introduced mass of water is equal to the optimal fill charge.

The variations of the curvature radius r_c are represented in Fig. 15. In the evaporator, because of the recession of the meniscus in the channel corners and the great difference of pressure between the two phases, the interfacial curvature radius is very small on the evaporator extremity. It is also noticed that the interfacial curvature radius decreases in the evaporator section when the heat flux rate increases. However, it increases in the condenser section. Indeed, when the heat input power increases, the liquid and vapor pressure losses increase, and the capillary pressure becomes insufficient to overcome the pressure losses. Hence, the evaporator becomes starved of liquid, and the condenser is blocked with the liquid in excess.

The evolution of the liquid and vapor pressures along the microchannel is given in Figs. 16 and 17. We note that the vapor pressure gradient along the microchannel is weak. It is due to the size and the shape of the microchannel that don't generate a very important vapor

pressure drop. For the liquid, the velocity increase is important near of the evaporator extremity, which generates an important liquid pressure drop.

Fig. 18 presents the evolution of the liquid phase velocity along a microchannel. In the evaporator section, as the liquid passage section decreases, the liquid velocity increases considerably. On other hand, since the liquid passage section increases along the microchannel (adiabatic and condenser sections), the liquid velocity decreases to reach zero at the final extremity of the condenser. In the evaporator, the vapor phase velocity increases since the vapor passage section decreases. In the adiabatic zone, it continues to grow with the reduction of the section of vapor passage. Then, when the condensation appears, it decreases, and it is equal to zero on the extremity of the condenser (Fig. 19).

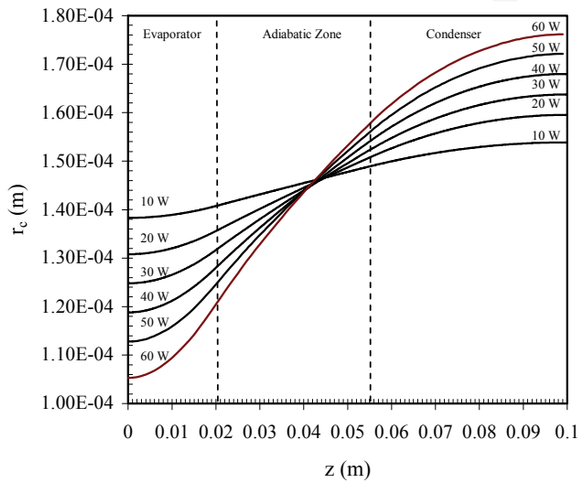

Fig. 15. Variations of the curvature radius r_c of the meniscus

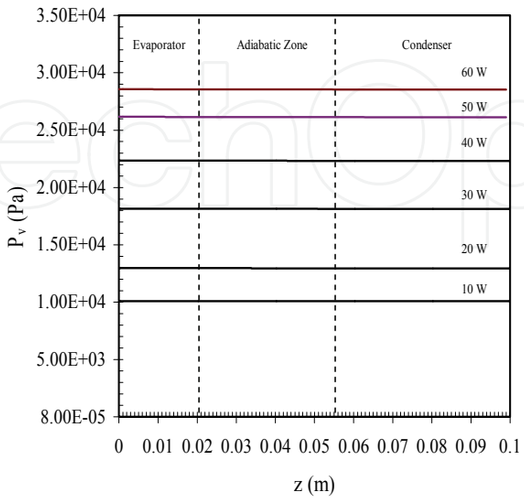

Fig. 16. Variations of the vapor pressure P_v

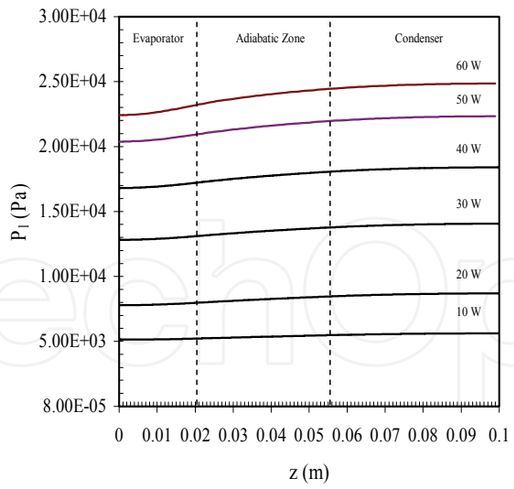

Fig. 17. Variations of the liquid pressure P_l

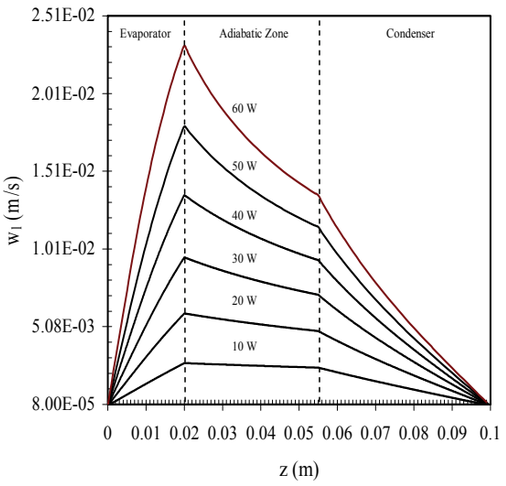

Fig. 18. The liquid phase velocity distribution

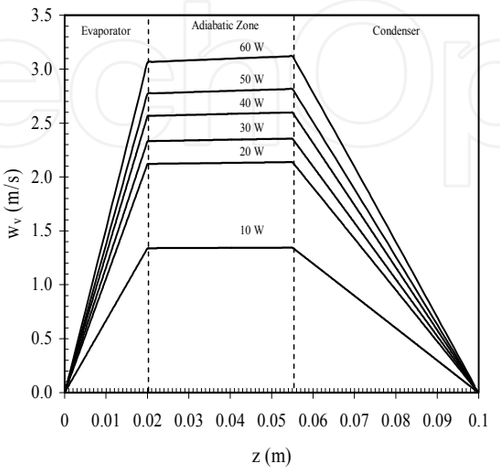

Fig. 19. The vapor phase velocity distribution

The variations of the wall temperature along the microchannel are reported in Fig. 20. In the evaporator section, the wall temperature decreases since an intensive evaporation appears due the presence of a thin liquid film in the corners. In the adiabatic section, the wall temperature is equal to the saturation temperature corresponding to the vapor pressure. In the condenser section, the wall temperature decreases. In this plot, are shown a comparison between the numerical results and the experimental ones, and a good agreement is found between the temperature distribution along the FMHP computed from the model and the temperature profile which is measured experimentally. An agreement is also noticed between the temperature distribution which is obtained from a pure conduction model and that obtained experimentally (Fig. 21).

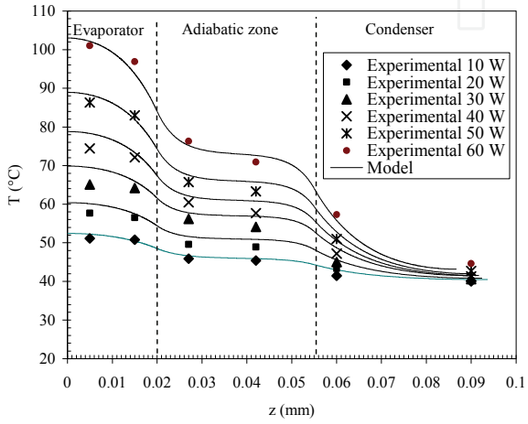

Fig. 20. Variations of the FMHP wall temperature

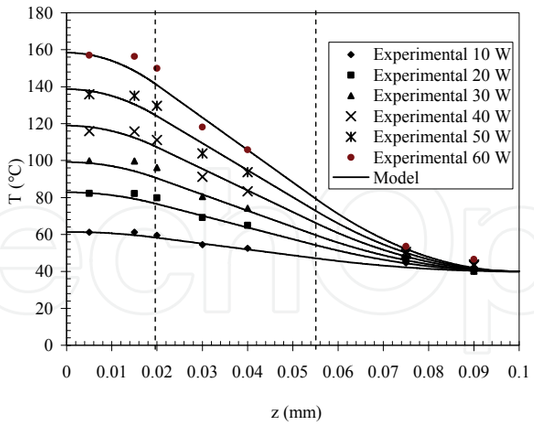

Fig. 21. Variations of the copper plate wall temperature

7. Conclusion

In this study, a copper FMHP is machined, sealed and filled with water as working fluid. The temperature measurements allow for a determination of the temperature gradients and maximum localized temperatures for the FMHPs. The thermal FMHP are compared to those

of a copper plate having the same dimensions. In this way, the magnitude of the thermal enhancement resulting from the FMHP could be determined. The thermal measurements show significantly reduced temperature gradients and maximum temperature decrease when compared to those of a copper plate having the same dimensions. Reductions in the source-sink temperature difference are significant and increases in the effective thermal conductivity of approximately 250 percent are measured when the flat mini heat pipes operate horizontally.

The main feature of this study is the establishment of heat transfer laws for both condensation and evaporation phenomena. Appropriate dimensionless numbers are introduced and allow for the determination of relations, which represent well the experimental results. This kind of relations will be useful for the establishment of theoretical models for such capillary structures.

Based on the mass conservation, momentum conservation, energy conservation, and Laplace-Young equations, a one dimensional numerical model is developed to simulate the liquid-vapor flow as well as the heat transfer in a FMHP constituted by microchannels. It allows to predict the maximum power and the optimal mass of the fluid. The model takes into account interfacial effects, the interfacial radius of curvature, and the heat transfer in both the evaporator and condenser zones. The resulting coupled ordinary differential equations are solved numerically to yield interfacial radius of curvature, pressure, velocity, temperature information as a function of axial distance along the FMHP, for different heat inputs. The model results predict an almost linear profile in the interfacial radius of curvature. The pressure drop in the liquid is also found to be about an order of magnitude larger than that of the vapor. The model predicts very well the temperature distribution along the FMHP.

Although not addressing several issues such as the effect of the fill charge, FMHP orientation, heat sink temperature, and the geometrical parameters (groove width, groove height or groove spacing), it is clear from these results that incorporating such FMHP as part of high integrated electronic packages can significantly improve the performance and reliability of electronic devices, by increasing the effective thermal conductivity, decreasing the temperature gradients and reducing the intensity and the number of localized hot spots.

8. References

Angelov, G., Tzanova, S., Avenas, Y., Ivanova, M., Takov, T., Schaeffer, C. & Kamenova, L. (2005). Modeling of Heat Spreaders for Cooling Power and Mobile Electronic Devices, *36th Power Electronics Specialists Conference (PESC 2005)*, pp. 1080-1086, Recife, Brazil, June 12-15, 2005

Avenas, Y., Mallet, B., Gillot, C., Bricard, A., Schaeffer, C., Poupon, G. & Fournier, E. (2001). Thermal Spreaders for High Heat Flux Power Devices, *7th THERMINIC Workshop*, pp. 59-63, Paris, France, September 24-27, 2001

Cao, Y., Gao, M., Beam, J.E. & Donovan, B. (1997). Experiments and Analyses of Flat Miniature Heat Pipes, *Journal of Thermophysics and Heat Transfer*, Vol.11, No.2, pp. 158-164

Cao, Y. & Gao, M. (2002). Wickless Network Heat Pipes for High Heat Flux Spreading Applications, *International Journal of Heat and Mass Transfer*, Vol.45, pp. 2539-2547

Chien, H.T., Lee, D.S., Ding, P.P., Chiu, S.L. & Chen, P.H. (2003). Disk-shaped Miniature Heat Pipe (DMHP) with Radiating Micro Grooves for a TO Can Laser Diode Package, *IEEE Transactions on Components and Packaging Technologies*, Vol.26, No.3, pp. 569-574

Do, K.H., Kim, S.J. & Garimella, S.V. (2008). A Mathematical Model for Analyzing the Thermal Characteristics of a Flat Micro Heat Pipe with a Grooved Wick, *International Journal Heat and Mass Transfer,* Vol.51, No.19-20, pp. 4637-4650

Do, K.H. & Jang, S.P. (2010). Effect of Nanofluids on the Thermal Performance of a Flat Micro Heat Pipe with a Rectangular Grooved Wick, *International Journal of Heat and Mass Transfer*, Vol.53, pp. 2183-2192

Gao, M. & Cao, Y. (2003). Flat and U-shaped Heat Spreaders for High-Power Electronics, *Heat Transfer Engineering,* Vol.24, pp. 57-65

Groll, M., Schneider, M., Sartre, V., Zaghdoudi, M.C. & Lallemand, M. (1998). Thermal Control of electronic equipment by heat pipes, *Revue Générale de Thermique*, Vol.37, No.5, pp. 323-352

Hopkins, R., Faghri, A. & Khrustalev, D. (1999). Flat Miniature Heat Pipes with Micro Capillary Grooves, *Journal of Heat Transfer*, Vol.121, pp. 102-109

Khrustlev, D. & Faghri, A. (1995). Thermal Characteristics of Conventional and Flat Miniature Axially Grooved Heat Pipes, *Journal of Heat Transfer,* Vol.117, pp. 1048-1054

Faghri, A. & Khrustalev, D. (1997). Advances in modeling of enhanced flat miniature heat pipes with capillary grooves, Journal of Enhanced Heat Transfer, Vol.4, No.2, pp. 99-109

Khrustlev, D. & Faghri, A. (1999). Coupled Liquid and Vapor Flow in Miniature Passages with Micro Grooves, *Journal of Heat Transfer*, Vol.121, pp. 729-733

Launay, S., Sartre, V. & Lallemand, M. (2004). Hydrodynamic and Thermal Study of a Water-Filled Micro Heat Pipe Array, *Journal of Thermophysics and Heat Transfer*, Vol.18, No.3, pp. 358-363

Lefèvre, F., Revellin, R. & Lallemand, M. (2003). Theoretical Analysis of Two-Phase Heat Spreaders with Different Cross-section Micro Grooves, *7th International Heat Pipe Symposium*, pp. 97-102, Jeju Island, South Korea, October 12-16, 2003

Lefèvre, F., Rullière, R., Pandraud, G. & Lallemand, M. (2008). Prediction of the Maximum Heat Transfer Capability of Two-Phase Heat Spreaders-Experimental Validation, *International Journal of Heat and Mass Transfer*, Vol.51, No.15-16, pp. 4083-4094

Lim, H.T., Kim, S.H., Im, H.D., Oh, K.H. & Jeong, S.H. (2008). Fabrication and Evaluation of a Copper Flat Micro Heat Pipe Working under Adverse-Gravity Orientation, *Journal of Micromechanical Microengineering,* Vol.18, 8p.

Lin, L., Ponnappan, R. & Leland, J. (2002). High Performance Miniature Heat Pipe, *International Journal of Heat and Mass Transfer*, Vol.45, pp. 3131-3142

Lin, J.C., Wu, J.C., Yeh, C.T. & Yang, C.Y. (2004). Fabrication and Performance Analysis of Metallic Micro Heat Spreader for CPU, *13th International Heat Pipe Conference*, pp. 151-155, Shangai, China, September 21-25, 2004

Moon, S.H., Hwang, G., Ko, S.C. & Kim, Y.T. (2003). Operating Performance of Micro Heat Pipe for Thin Electronic Packaging, *7th International Heat Pipe Symposium*, pp. 109-114, Jeju Island, South Korea, October 12-16, 2003

Moon, S.H., Hwang, G., Ko, S.C. & Kim, Y.T. (2004). Experimental Study on the Thermal Performance of Micro-Heat Pipe with Cross-section of Polygon, *Microelectronics Reliability*, Vol.44, pp. 315-321

Murakami, M., Ogushi, T., Sakurai, Y., Masumuto, H., Furukawa, M. & Imai, R. (1987). Heat Pipe Heat Sink, *6th International Heat Pipe Conference*, pp. 257-261, Grenoble, France, May 25-29, 1987

Ogushi, T. & Yamanaka, G. (1994). Heat Transport Capability of Grooves Heat Pipes, *5th International Heat Pipe Conference*, pp. 74-79, Tsukuba, Japan, May 14-18, 1994

Plesh, D., Bier, W. & Seidel, D. (1991). Miniature Heat Pipes for Heat Removal from Microelectronic Circuits, *Micromechanical Sensors, Actuators and Systems*, Vol.32, pp. 303-313

Popova, N., Schaeffer, C., Sarno, C., Parbaud, S. & Kapelski, G. (2005). Thermal management for stacked 3D microelectronic packages, *36th Annual IEEE Power Electronic Specialits Conference (PESC 2005)*, pp. 1761-1766, recife, Brazil, June 12-16, 2005

Popova, N., Schaeffer, C., Avenas, Y. & Kapelski, G. (2006). Fabrication and Experimental Investigation of Innovative Sintered Very Thin Copper Heat Pipes for Electronics Applications, *37th IEEE Power Electronics Specialist Conference (PESC 2006)*, pp. 1652-1656, Vol. 1-7, Cheju Island, South Korea, June 18-22, 2006

Romestant, C., Burban, G. & Alexandre, A. (2004). Heat Pipe Application in Thermal-Engine Car Air Conditioning, *13th International Heat Pipe Conference,* pp. 196-201, Shanghai, China, September 21-25, 2004

Schneider, M., Yoshida, M. & Groll, M. (1999a). Investigation of Interconnected Mini Heat Pipe Arrays For Micro Electronics Cooling, *11th International Heat Pipe conference,* 6p., Musachinoshi-Tokyo, Japan, September 12-16, 1999

Schneider, M. Yoshida, M. & Groll, M. (1999b). Optical Investigation of Mini Heat Pipe Arrays With Sharp Angled Triangular Grooves, *Advances in Electronic Packaging*, EEP-Vol. 26-1 and 26-2, 1999, pp. 1965-1969.

Schneider, M. Yoshida, M. & Groll, M. (2000). Cooling of Electronic Components By Mini Heat Pipe Arrays, *15th National Heat and Mass transfer Conference and 4th ISHMT/ASME Heat and Mass Transfer Conference, 8p.,* Pune, India, January 12-14, 2000

Soo Yong, P. & Joon Hong, B. (2003). Thermal Performance of a Grooved Flat-Strip Heat Pipe with Multiple Source Locations, *7th International Heat Pipe Symposium*, pp. 157-162, Jeju Island, South Korea, October 12-16, 2003

Shi, P.Z., Chua, K.M., Wong, S.C.K. & Tan, Y.M. (2006). Design and Performance Optimization of Miniature Heat Pipe in LTCC, *Journal of Physics: Conference Series*, Vol.34, pp. 142-147

Sun, J.Y. & Wang, C.Y. (1994). The Development of Flat Heat Pipes for Electronic Cooling, *4th International Heat Pipe Symposium*, pp. 99-105, Tsukuba, Japan, May 16-18, 1994

Tao, H.Z., Zhang, H., Zhuang, J. & Bowmans, J.W. (2008). Experimental Study of Partially Flattened Axial Grooved Heat Pipes, *Applied Thermal Engineering*, Vol.28, pp. 1699-1710

Tzanova, S., Ivanova, M., Avenas, Y. & Schaeffer, C. (2004). Analytical Investigation of Flat Silicon Micro Heat Spreaders, *Industry Applications Conference, 39th IAS Annual Meeting Conference Record of the 2004 IEEE*, pp. 2296-2302, Vol.4, October 3-7, 2004

Xiaowu, W., Yong, T. & Ping, C. (2009). Investigation into Performance of a Heat Pipe with Micro Grooves Fabricated by Extrusion-Ploughing Process, *Energy Conversion and Management*, Vol.50, pp.1384-1388

Zaghdoudi, M.C. & Sarno, C. (2001). Investigation on the Effects of Body Force Environment on Flat Heat Pipes, *Journal of Thermophysics and Heat Transfer*, Vol.15, No.4, pp. 384-394

Zaghdoudi, M.C., Tantolin, C. & Godet, C. (2004). Experimental and Theoretical Analysis of Enhanced Flat Miniature Heat Pipes, *Journal of Thermophysics and Heat Transfer*, Vol.18, No.4, pp. 430-447

Zhang, L., Ma, T., Zhang, Z.F. & Ge, X. (2004). Experimental Investigation on Thermal Performance of Flat Miniature Heat Pipes with Axial Grooves, *13th International Heat Pipe Conference*, pp. 206-210, Shangai, China, September 21-25, 2004

Zhang, M., Liu, Z. & Ma, G. (2009). The Experimental and Numerical Investigation of a Grooved Vapor Chamber, *Applied Thermal Engineering*, Vol.29, pp. 422-430

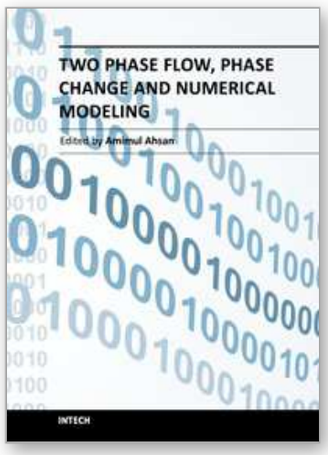

Two Phase Flow, Phase Change and Numerical Modeling
Edited by Dr. Amimul Ahsan

ISBN 978-953-307-584-6
Hard cover, 584 pages
Publisher InTech
Published online 26, September, 2011
Published in print edition September, 2011

The heat transfer and analysis on laser beam, evaporator coils, shell-and-tube condenser, two phase flow, nanofluids, complex fluids, and on phase change are significant issues in a design of wide range of industrial processes and devices. This book includes 25 advanced and revised contributions, and it covers mainly (1) numerical modeling of heat transfer, (2) two phase flow, (3) nanofluids, and (4) phase change. The first section introduces numerical modeling of heat transfer on particles in binary gas-solid fluidization bed, solidification phenomena, thermal approaches to laser damage, and temperature and velocity distribution. The second section covers density wave instability phenomena, gas and spray-water quenching, spray cooling, wettability effect, liquid film thickness, and thermosyphon loop. The third section includes nanofluids for heat transfer, nanofluids in minichannels, potential and engineering strategies on nanofluids, and heat transfer at nanoscale. The forth section presents time-dependent melting and deformation processes of phase change material (PCM), thermal energy storage tanks using PCM, phase change in deep CO2 injector, and thermal storage device of solar hot water system. The advanced idea and information described here will be fruitful for the readers to find a sustainable solution in an industrialized society.

How to reference
In order to correctly reference this scholarly work, feel free to copy and paste the following:

Zaghdoudi Mohamed Chaker, Maalej Samah and Mansouri Jed (2011). Theoretical and Experimental Analysis of Flows and Heat Transfer Within Flat Mini Heat Pipe Including Grooved Capillary Structures, Two Phase Flow, Phase Change and Numerical Modeling, Dr. Amimul Ahsan (Ed.), ISBN: 978-953-307-584-6, InTech, Available from: http://www.intechopen.com/books/two-phase-flow-phase-change-and-numerical-modeling/theoretical-and-experimental-analysis-of-flows-and-heat-transfer-within-flat-mini-heat-pipe-includin

InTech Europe
University Campus STeP Ri
Slavka Krautzeka 83/A
51000 Rijeka, Croatia
Phone: +385 (51) 770 447
Fax: +385 (51) 686 166
www.intechopen.com

InTech China
Unit 405, Office Block, Hotel Equatorial Shanghai
No.65, Yan An Road (West), Shanghai, 200040, China
中国上海市延安西路65号上海国际贵都大饭店办公楼405单元
Phone: +86-21-62489820
Fax: +86-21-62489821

IntechOpen